RESEARCH ARTICLE

Key Points:
- The interaction of multiple source flows is modeled using complex potentials
- Algorithms are given for lava flows, salt sheets, and oil migration
- The Chao lava field model uses three major vents

Correspondence to:
R. Weijermars,
R.Weijermars@TUDelft.nl

Visualization of space competition and plume formation with complex potentials for multiple source flows: Some examples and novel application to Chao lava flow (Chile)

R. Weijermars[1,2,3]

[1]Bureau of Economic Geology, University of Texas at Austin, Austin, Texas, USA, [2]Department of Geoscience and Engineering, Delft University of Technology, Delft, Netherlands, [3]Alboran Energy Strategy Consultants, Delft, Netherlands

Abstract Fluid displacement in a continuum pressured by a variable constellation of source flows can be visualized as solutions of line integrals. The algorithms are based on complex potentials that provide exact solutions of the Navier-Stokes equation and allow users to specify both the location and flux strength of multiple sources. If relative strength and positioning of the sources are varied, a wide range of flow patterns and particle paths can be traced. Time-dependent variations in the strength of the sources can account for transient-flow problems. A further expansion is superposition of a background flow, which displaces the particle paths issued from the sources into concentrated plumes. The outlined modeling technique for visualization of multiple plume displacements is potentially relevant for a wide spectrum of practical situations. Detailed applications are possible, such as time tracking of groundwater-plume migration from a series of pollution sources, tracking of salt-feeder-stock flow and suture zone formation when salt issued from the stocks coalesces into a salt canopy, and designing of optimal spacing and relative pressure strength of multiple water injection wells in field-development plans for hydrocarbon production. Further applications are highlighted in the main text, including a simulation of geometrical features exposed in the Chao coulee (Chilean Andes).

1. Introduction

Advanced numerical analyses of nonlinear flow solutions have been enabled by computational methods to solve the differential equations by approximate solutions [*Anderson*, 1995]. As a result, fluid mechanics has shifted over the past couple of decades from analytical solutions of linear flow (exact solutions of approximate flow descriptions—as boundary conditions are often simplified) to numerical methods of solving nonlinear differential equations (approximate solutions of more realistic problems—as more detailed boundary conditions can be built in [cf. *Drazin and Riley*, 2006]). Analytical descriptions remain useful for describing linear flow systems because exact solutions of the Navier-Stokes equation elucidate the fundamentals of fluid flow [*Barenblatt*, 1996]. A new depth of analytical descriptions with exact flow simulations of sophisticated flow geometries can be realized when modern computer power is exploited. The exact analytical solutions thus obtained can provide a suitable alternative for, or complement to, numerical-flow-visualization methods.

This study focuses on the visualization of progressive growth of multiple source flows, each scaled for various strengths, based on 2-D analytical descriptions, with and without a superimposed far-field uniform flow. The algorithms are valid for incompressible fluids (vanishing divergence) and irrotational flows (vanishing curl), which means that free-slip is assumed at any physical boundary. Our analytical models are equally valid for flow in viscous and inviscid fluids, provided the study area is sufficiently far from boundary-layer effects. Under these assumptions, divergence of the flow lines relates to spatial changes in the physical pressure gradient and leads to velocity deceleration, whereas acceleration occurs for convergent flow lines. The viscous-flow assumption can be ascertained as long as boundary-layer effects are negligible (or located far enough away to justify their being neglected). For a detailed analytical description of boundary-layer effects, see a review by *Wang* [1991].

We visualize the fluid displacement of fluid issued from sources, which provides insight into the competition for flow space between multiple sources of various flux strengths. The standard application of this method is for steady state flow. Slow variation of the rate of the source is acceptable in a quasi-steady state approximation, when the time scale for the parameter variation is large compared to the time scale of the

fluid flow inside the domain. The basic analytical description of steady linear flow from a source holds when introducing a time-dependent source strength in a high-viscosity medium, and thereby our analytical models can account for nonlinear progression of particle paths. This assumes storage of fluid is negligible, i.e., the continuum remains uniformly occupied by a constant density fluid. Moreover, since the method neglects the nonlinear terms in the Navier-Stokes equation, the superposition principle applies. A uniform flow can be superposed, which simulates a further pressure gradient that alters the flow and line integrals for the flow space but not the density of the fluid; inertia effects are excluded. A solid framework for our present analysis is provided by a concise summary of the fundamental equations (Appendices A and B). This theoretical framework also offers a convenient foundation for advanced future studies.

The algorithms developed here have considerable practical value for a range of geophysical applications. Although potential theory has been widely applied to groundwater flow, hydrocarbon field flooding (see section 2; and electrodynamics and aeronautics, not further addressed here) application to other geophysical flows has not been attempted. Concise examples of multiple source flow visualizations are included here (section 3), enabled by modern computing power in combination with carefully selected model parameters. This study concludes with a new application to transient lava flows emerging from three eruption vents while they compete for space and engulf one another, like those mapped of the Chao dacite lava fields in the Chilean Andes (see section 4), followed by a discussion (section 5) and conclusions (section 6).

2. Previous Fundamental Work

Source flows enjoy the attention of applied mathematicians because they can be described by concise functions with analytical solutions. Streamlines may be visualized by a mapping of complex contour integrals using the vector field representation of complex variables, as formalized by Pólya [*Pólya and Latta*, 1974]. A similar method has been used in fluid mechanics that employs complex functions for concise mathematical representation of potential and stream functions [*Batchelor*, 1967; *Weijermars and Poliakov*, 1993; *Kundu and Cohen*, 2002]. These functions can describe the physical transport of particles in basic flow fields (vortices, sources, sinks, doublets, and uniform flows). Alternatively, simple analytical equations for characterizing velocity vectors around source flows perturbed by a superposed uniform far-field flow (following equations introduced by Rankine) are available in fluid-mechanics literature [*White*, 2011].

A good number of flows can be described by combining appropriate pairs of potential functions and stream functions that satisfy Cauchy-Riemann equations. To be valid solutions of the Navier-Stokes equation, the analytical descriptions assume the following: (1) conservation of mass, which means that the divergence must be zero and that it adopts incompressibility, and (2) irrotational flow, so that vorticity (also termed *curl* or *circulation*) is zero, which is best defensible when the model fluid is an inviscous continuum. The two assumptions of (1) an inviscous fluid and (2) a continuum are often seen as limiting the practical application of flow descriptions by potential theory, which may explain why no applications have been attempted to flows of very high viscosity fluids. The common misperception that potential flow and stream function descriptions would only apply to inviscous fluids probably follows from an overly cautious approach: inviscous fluids will always flow in irrotational fashion and therefore automatically fulfil the requirements of potential flow. *Joseph* [2006] has explained in detail why this interpretation is incorrect: irrotational flow is a property of the flow, and viscosity is a property of the material; irrotational flows may occur in both viscous and inviscous fluids. An elegant example of an irrotational flow is Couette flow; as follows from its equation of motion $\nabla^2 = 0$, the curl (vorticity) vanishes. Couette flow is certainly not restricted to inviscous fluids and is exploited in many fluid mechanical devices to measure the dynamic shear viscosity. Concise complex potential and stream function descriptions for Couette flow are available [*Weijermars and Poliakov*, 1993].

Potential flow theory can be applied, without any adaptations, to many flows involving incompressible, viscous fluids [*Joseph and Liao*, 1994; *Joseph*, 2003, 2006; *Joseph et al.*, 2007]. More specifically, *Joseph* [2006] states "Every theorem about potential flow of perfect fluids with conservative body forces applies equally to viscous fluids in regions of irrotational flow." A more relaxed formulation is given in a related study [*Joseph et al.*, 2007]: "Viscous potential flow is a potential flow solution of the Navier-Stokes equation in which the vorticity vanishes and no-slip conditions at interface are not enforced." One could amplify that if solid boundaries (interfaces) are not occurring near the flow region studied, the flow description is valid for an infinite viscous continuum for which conditions of no-slip do not appear relevant.

Viscous fluids can be described by exact analytical solutions as long as boundary-layer effects are negligible or provide approximate solutions if boundary layers do develop. The continuum requirement can be modified as well. If no boundaries are introduced, the fluid space remains infinite with no boundary effects. But the presence of solid (but free-slip) boundaries can be accounted for by skillful simulation of boundary conditions with complex analysis, such as the mirror-imaging technique and conformal mapping of flows in confined regions with zero flux across one or more of the confined borders (see, e.g., Appendix B, Figures B2a and B2b).

The key property of analytical functions of complex line integrals is that the complex variables map the spatial position of the complex function and the variables also describe valid solutions for fluid flow in each position. For detailed definitions of analytical functions and line integrals, see *Needham* [1997, p. 197 and 383, respectively]. Numerous introductions and advanced texts on conformal mapping are readily available [*Churchill and Brown*, 1984; *Potter*, 2008; *Zill and Shanahan*, 2009; *Brilleslyper et al.*, 2012]. Brief introductory articles on line integrals and complex analysis with a popular slant may provide useful entry-level reading for students [*Braden*, 1987; *Gluchoff*, 1993; *Wegert and Semmler*, 2011], which could be followed by studies discussing complex analysis of 3-D flows requiring advanced mathematical skills [*Kelly et al.*, 1990; *Shaw*, 2010].

Specific examples of applications of potential theory and conformal mapping to groundwater flows and hydrocarbon reservoir models abound. One suite of potential applications is in groundwater-plume migration models aimed at forensic backtracking to locate the single or multiple source(s) of pollution. Another major application area is in the design of optimal spacing and relative strength of water injection wells for enhanced recovery of hydrocarbons (or for optimizing fluid circulation in geothermal-energy projects). Specific applications of potential theory to a continuum invaded by a pore fluid, such as Darcy flow in a homogeneous granular medium in each disciplinal domain, are recommended—e.g., for groundwater flow [*Haitjema*, 1995; *Haitjema et al.*, 2010; *Strack*, 1989, 2003] and for reservoir models [*Hurst*, 1991; *Chin*, 2002; *Jha et al.*, 2012]. The present study builds on such tools and focuses on the interaction of multiple sources with a far-field superposed flow that includes transient flow due to time-dependent flux strengths in high-viscosity materials, which moves the theory into new territory.

3. Modeling Tools and Generic Examples

3.1. Modeling Tools

For the superposition of multiple source flows in analytical models, complex potentials and flow mapping in the complex plane provide powerful tools. The *z* plane is a geometric representation using the real axis and the orthogonal imaginary axis, with the real part of a complex number represented by a position along the *x* axis and the imaginary part along the *y* axis. Complex analysis is here applied so that examples of an infinite range of 2-D flow patterns that may occur when source flows of different strengths and varying positions interact may be visualized. The superposition of far-field flow is also systematically modeled. All results are visualized using Matlab code on the basis of a suite of equations. Mathematical tools such as the potential function, stream function, and complex potential are concisely outlined in Appendix A. The more specific mathematics of deriving complex potentials for multiple source flows is stepwise developed in Appendix B.

3.2. Multiple 2-D Sources Without Far-Field Flow

The principal effect of varying the relative strength of any one or a number of multiple extrusion points (fluid sources; as opposed to fluid vanishing in sinks) can be visualized by a stepwise increase of the flux strength of one of four sources (Figures 1a–1d). The location of all four sources is arbitrary but corresponds precisely to a basic case modeled in an earlier, independent study [*Potter*, 2008]—for a combination of two sources and two sinks. This basic case was used to validate—as a starting point—our code by exactly reproducing with our code the earlier, independent result, which is included in Appendix B as Figure B2b. The advanced simulations of Figures 1a–1d demonstrate that the number and width of flow path tubes for the source with the weakest flux (located in the origin) is drastically reduced when the flux of the source in the upper left corner of the flow region is progressively turned on from moderate to full strength (compare the time series of Figures 1a–1d with the relevant flux rate increasing from 1.5 via 3 to 6 to 10, respectively). When the upper left source is turned on at full flux rate, fluid emanating from the weakest source in the origin is no longer spreading into three distinct flow lanes but becomes confined to flow in just one lane, moving to the lower right corner (Figure 1d).
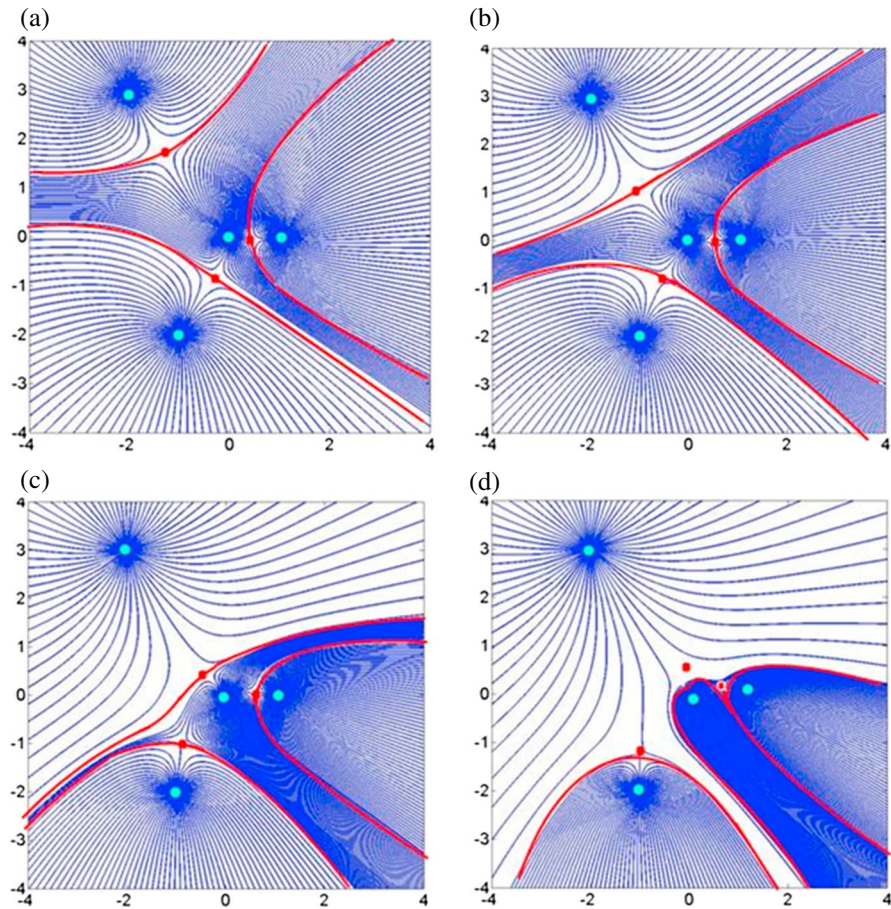
Figure 1. Streamlines (blue curves) for the steady flow fields around four injection sources (light blue dots) located in the complex plane at $z = 0, 1, -1 - 2i, -2 + 3i$. The nondimensional flux strengths of these respective sources is (a) 0.5, 1, 2, and 1.5; (b) 0.5, 1, 2, and 3; (c) 0.5, 1, 2, and 6; (d) 0.5, 1, 2, and 10. Red curves separate flows issued from each source. Red dots are stagnation points of zero flow rate.

Spread of fluid issued by individual plumes is contoured for equal time steps (Figures 2a and 2b). The stronger sources have widely spaced contours, and the weaker sources displace the source fluid much more slowly. Each of the cases in Figures 2a and 2b is steady state flow, for which streamlines and stagnation points do not shift over time. The motion of fluid particles is uniquely described by their departure position $z(t_0) = z_0 = x_0 + iy_0$ at an initial time t_0 and subsequent positions $z(t)$. For stagnation points, the solution for any time $z(t)$ remains a constant z_0 [*Olver*, 2012].

A further option in the developed model allows for time-dependent decay (or growth) of injected-source flux rates. For sources with flux strengths varying over time, particle paths can be traced by solutions $z(t)$, and these are scaled solely by flux strength (m). Figure 3 shows flow paths when flux from the initially strongest source in the upper left corner is progressively weakening (by a decline function). Fluid issued from its source is first halted (when the source dies), and subsequently the fluid (that earlier emanated from the source) begins to recede toward its original source. Particles emanating from the source at two different times will follow different flow paths; both of their solutions are analytic and differentiable.

The approach illustrated in Figures 1 through 3 can be used to model flow paths proactively in hydrocarbon reservoirs that must be depleted by strategic positioning of water injection wells having varying pressures (that control the fluxes). Smart regulation of relative pressures in such wells can then be manipulated to maximize the recovery of oil by waterflooding of oil reservoirs. Another obvious application of the model tool is in forensic reconstructions of groundwater pollution when a range of possible sources are interacting. The model can pinpoint the main source(s) of pollution on the basis of concentration of pollutants in the various
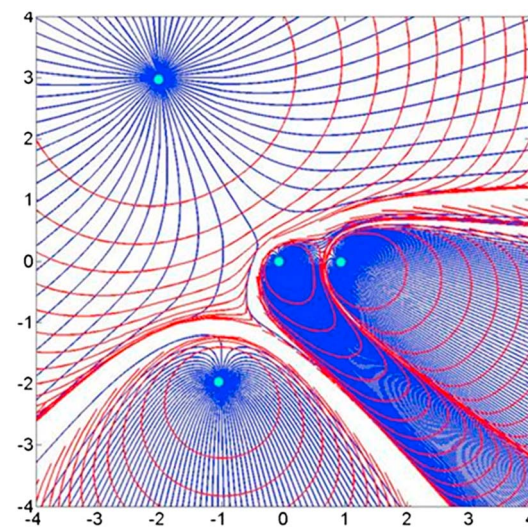
(a)   (b)
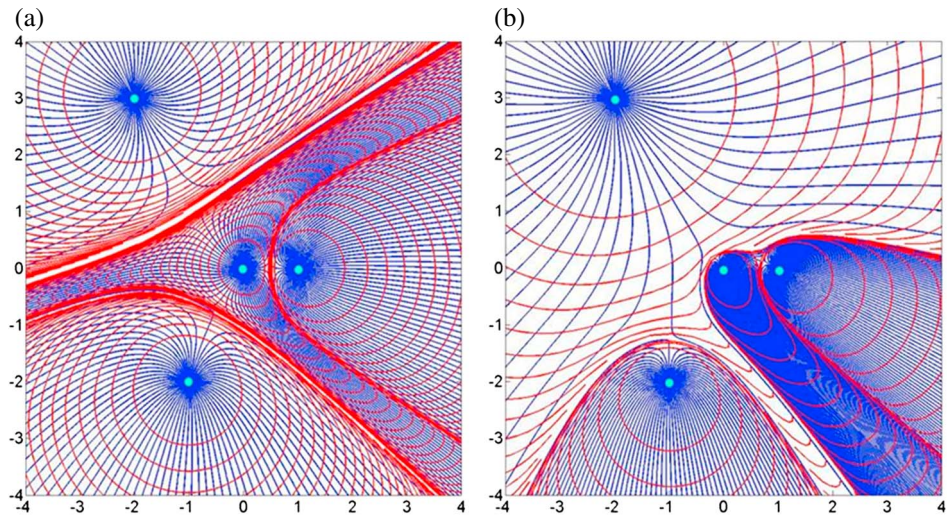
Figure 2. Nondimensional time contours for $\Delta t^* = 0.2$ (red) showing differential travel speed of fluid particles emanating from each source (total runtime $t^* = 5$). Particle paths are mapped using velocity equations developed in Appendix B. Locations of sources are identical to those in Figure 1. Source fluxes are (a) as in Figure 1b and (b) as in Figure 1d.

sectors. Pollutant concentration will be highest for the weakest source, provided initial concentration of the pollutant fluid is equal for all sources.

### 3.3. Multiple 2-D Sources With Uniform Background Flow

We next use the principle that any number of complex potentials, velocity potentials, stream functions, and potential functions (see Appendix A for basics) of different superimposed flows can be summed to then provide valid solutions to the continuum assumption and compatibility requirements. The flow space occupied by multiple source flows can be attacked by a background flow maintained by a regional pressure gradient. First,

Figure 3. Transient flow with particle paths (blue curves) of fluid issued at $t^* = 0$ from four injection sources (light dots) located in the complex plane at $z = 0, 1, -1 - 2i, -2 + 3i$. The nondimensional flux strengths of the respective sources are 0.5, 1, 2, and $10(10^*d)^t$, with decline factor $d = -0.2$. Nondimensional time contours (red) are for $\Delta t^* = 0.2$ and show differential travel speed of fluid particles emanating from each source (total runtime $t^* = 5$).

two sources with equal flux strengths are each contoured for fluid displacement at evenly spaced time steps (Figure 4). This flow may apply to practical situations in which liquid is injected via two adjacent wells into a subsurface reservoir (e.g., carbon dioxide injected for sequestration into an aquifer or any other liquid injected at laminar flow speeds into a subhorizontal reservoir). It should be noted that in our flow simulation we have neglected the effect of storage, which remain important when pore space is incompletely filled in Darcy flow of undersaturated aquifers [*Haitjema*, 1995; *Strack*, 1989]. Storage would also need to be taken into account in applications to undersaturated hydrocarbon and geothermal reservoirs, but in our examples saturation is assumed.

The same two source flows of Figure 4 can be forcefully deflected by the superposition of a strong pressure gradient that maintains a "draft" flow, and distortion of the plumes depends on the direction and relative speed of the background flow (Figures 5a and 5b). The flux rate of the two sources (Figures 5a and 5b) are all identical, but the background flow comes in from the top in
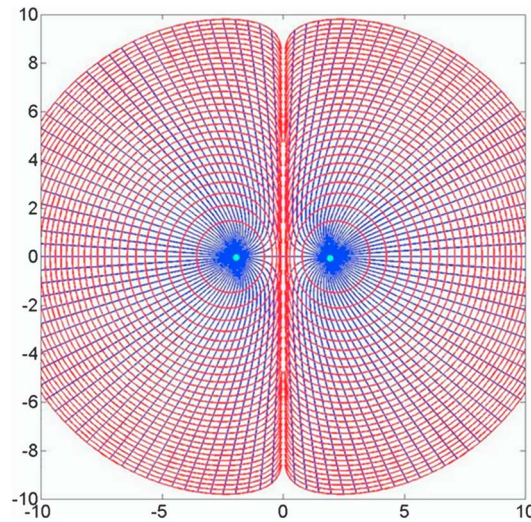
Figure 4. Two sources juxtaposed with equal flux strength (1, 1) located at $z = (-2, +2)$ and time contours (red curves) are mapped for spacing $\Delta t^* = 1$ and total nondimensional runtime $t^* = 30$. No far-field flow is superposed.

Figure 5a and from the left in Figure 5b and illustrates how plume geometry may differ as a result of variations in the gradient direction of the background flow.

The effect of far-field flow on the plumes can be reduced by increasing the injection rate of the two sources, which is equivalent to reducing the background flow rate in our model (Figure 6). Manipulation of the various rates can bring the two plumes back to coalescence so that the full background flow will be deflected around the two coalesced plumes (Figure 6). This injection strategy can be helpful in creating a Rankine-like flow profile around a cluster of injection wells. Conversely, a far-field waterflood may be used to engulf an oil-saturated patch in a hydrocarbon reservoir around two production wells.

Further manipulation of subsurface flows is possible if one of the injectors is rendered weaker than the nearby injection source so that the weaker source plume becomes shielded from intermingling by the background flow (Figure 7). This manipulation may be a useful strategy when a particular fluid or foam would be reactive to chemical agents in the far-field flow and would need to be kept segregated. An interesting application also emerges in geothermal-energy management by forceful confinement of fluids into streams using thermal layering, which requires smart well placement and well-rate control so as to ensure maximum energy production from the circulated fluid. Such an approach can provide a smart field-management tool if well pumps are hooked up to the governing algorithms. Well pressures can then be manipulated to establish the initial flow plan, and adjustments can be made when production data from the wells prompt for another desirable flow pattern. Although applications of complex potentials to ground water flow [*Haitjema*, 1995; *Haitjema et al.*, 2010; *Strack*, 1989, 2003] and hydrocarbon reservoirs [*Hurst*, 1991; *Chin*, 2002; *Jha et al.*, 2012] have been developed before, the above visualizations are unique in that they include carefully scaled migration fronts of the injected fluid.
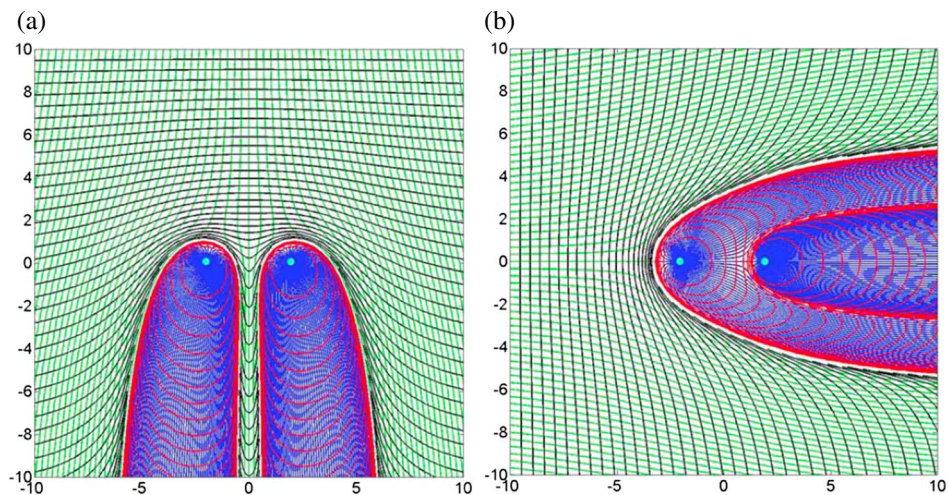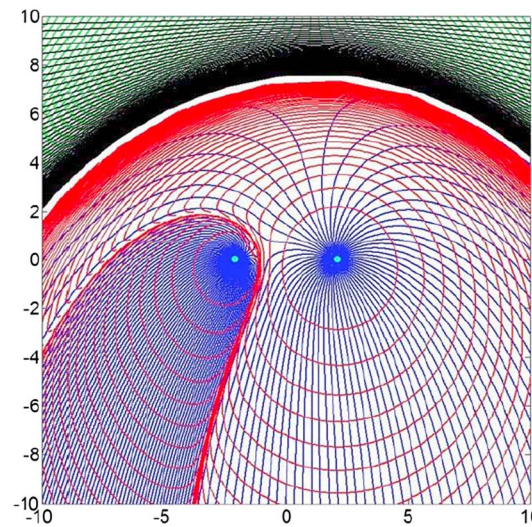

Figure 5. Two sources of equal flux strength (1, 1) located at $z = (-2, +2)$ attacked by background flow (green: flow lines, black: timelines) with speed and direction. (a) $(u_x, u_y) = (0, -1)$ and (b) $(u_x, u_y) = (1, 0)$. Nondimensional time contours for $\Delta t^* = 0.6$ (red and black curves) show differential travel speed of fluid particles (total runtime $t^* = 30$).
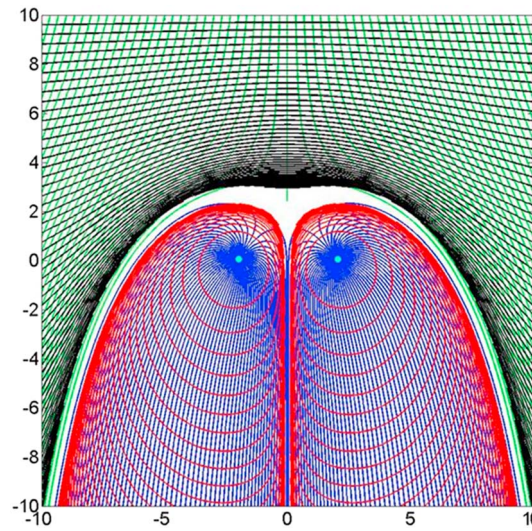
Figure 6. Two sources of equal flux strength (1, 1) located at $z = (-2, +2)$ attacked by a background flow (green: flow lines, black: timelines) with speed and direction: $(u_x, u_y) = (0, -0.5)$. Nondimensional time contours for $\Delta t^* = 1$ (red and black curves) show differential travel speed of fluid particles (total runtime $t^* = 75$). White space indicates that tracked fluid particles have not reached this fluid space within the monitored runtime.

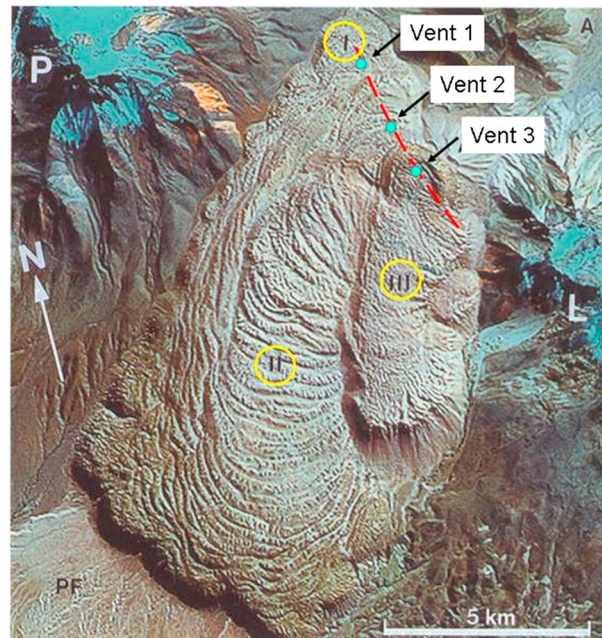## 4. High-Viscosity Flow Application

4.1. Basic Features of Chao Coulee

The application of theoretical model of source flows outlined above can now be expanded to mimic the basic flow features observed in terrestrial lava flows. The Chao dacite in the Atacama Desert of the Chilean Andes embodies one of the largest examples on Earth of a coulee— a flow of viscous lava with a blocky appearance (Figure 8). The Chao coulee, 14.5 km long with flow fronts 350 to 400 m high, represents a total erupted volume of approximately 26 km³ [*de Silva et al.*, 1994]. Characteristic features on the surface of the coulee are the prominent 30 m high flow ridges resulting from folding of the surface layers that are due to differential cooling (which makes the surface layers stiffer as a result of the viscosity that is higher than that of the underlying hotter lava) while the lava sheet advanced [*Guest and Sanchez*, 1969; *de Silva et al.*, 1994]. The Chao dacite flow was previously mapped into three zones (I, II, and II in Figure 8) corresponding to distinct eruption stages [*de Silva et al.*, 1994]. The three lava fields are here interpreted to be issued from three principal vents situated in a topographical saddle between the Léon and Paniri volcanoes and aligned on an inferred radial-tension fracture originating from one of the nearby volcanoes (fracture marked by red trace in Figure 8). An early explosive effusion of dacitic ignimbrites (<1 km³) was followed by eruptions of the main Chao I and II lava fields (~ 22 km³). A lava surge from the third eruption vent emplaced the Chao III lava field (~3 km³) and was preceded by formation of a dense pumice cone and effusion of rhyolitic tephra. The Chao lava composition is high in potassium and very porphyritic, indicating slow cooling. The entire Chao lava complex is thought to have erupted less than 100,000 years ago, possibly within a brief period of 100 to 150 years [*de Silva et al.*, 1994].

4.2. Emplacement Model for Chao Coulee

Relative fluxes, starting times, and cessation of lava flows emanating from the three Chao vents were modulated in our model until a satisfactory resemblance was achieved with the mapped lava fields. Flow in the basal part of the lava flows will be influenced by preexisting topography, but the upper lava layers may flow over the basal layers and assume the lava-plume shape controlled by the flux strength of the source vents relative to the superposed downslope speed. The two principal axes of the complex z plane (x, iy) were aligned with the margins of the satellite image (Figure 8). The middle vent is located at $z = 0$, and the two other vents are at $z = -1 + 2i$ and $z = 1 - 2i$, respectively.

The features of the model (Figure 9) closely resemble the morphological features observed in the three principal Chao lava fields. The optimal

Figure 7. Two sources of unequal flux strength (1, 3) located at $z = (-2, +2)$ attacked by background flow (green: flow lines, black: timelines) with speed and direction: $(u_x, u_y) = (0, -0.5)$. Nondimensional time contours for $\Delta t^* = 1$ (red and black curves) show differential travel speed of fluid particles (total runtime $t^* = 30$). Filling in the white space with fluid that left the sources at $t^* = 0$ would require much longer runtime.

Figure 8. Satellite image of compounded lava fields Chao I, II, and III set amidst the Léon volcano (L) and Paniri volcano (P) with ash cones (A) and pumice field (PF) [after *de Silva et al.*, 1994]. The three major Chao eruption vents are marked along an inferred radial-tension fracture that probably originated from one of the nearby volcanoes.
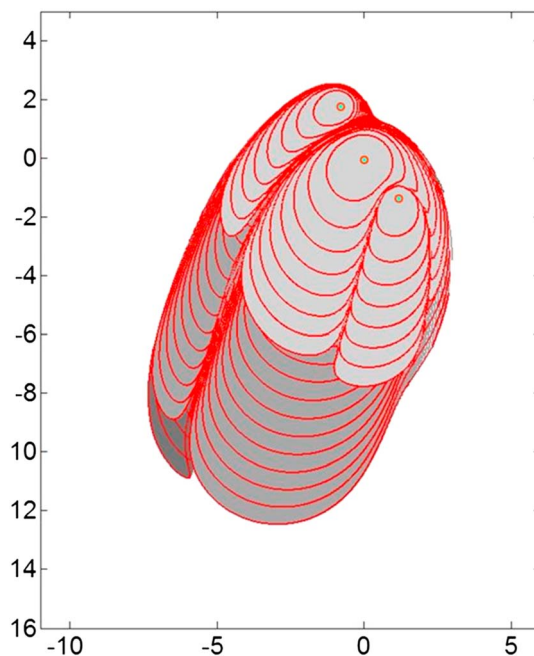
Figure 9. Fluid issued from three vents (light dots) in the complex plane at $z = -0.8 + 1.8i$, $z = 0$, and $z = 1.1 - 1.3i$. Their nondimensional flux strengths are 0.2, 0.6, and 0.3, respectively. Red contours are timelines for each $\Delta t^* = 1$. The superimposed gravity-driven, far-field flow is $(u_x, u_y) = (-0.16, -0.5)$. Different gray shades highlight lava issued from vent 1 starting at $t^* = 0$ (dark gray), vents 1 and 2 starting at $t^* = 2$ (medium gray), and from vents 1, 2, and 3 starting at $t^* = 12$ (light gray).

match with the three major Chao lava fields could be achieved when the relative flux strengths of the vents in the model were set at $m_1 = 0.2$ for $z = -0.8 + 1.8i$, $m_2 = 0.6$ for $z = 0 + i0$, and $m_3 = 0.3$ for $z = 1.1 - 1.3i$. A sequential onset of the source fluxes in our model provided the best match to the geometry of the observed outlines of the Chao lava fields and mimics the curvature of its ogives. Fluxes from m_1, m_2, and m_3 sources were started in consecutive order at distinct nondimensional flow times $t_1^* = 0$ for m_1, $t_2^* = 2$ for m_2, and $t_3^* = 12$ for m_3. All three sources ceased their flow at $t^* = 20$. The background flow rate $U_\infty = 0.28$ was superimposed on the source flows with the setting of $(u_x, u_y) = (-0.16, -0.5)$. In nature, the far-field flow rate is controlled by the topographical slope of the terrain and the viscosity and density of the lava.

Our model parameters indicate that magmatic vents in the natural prototype were most likely activated one after the other as a result of progressive widening of space between the walls of the fracture along which the vents are located. Progressive widening of the fracture plane southeastward suggests that the fracture propagated in this direction from a principal stress source that initiated the fracture in the northwest. In Figure 9, each shade of gray corresponds to the onset of a vent: dark gray shows that the lava flow issued after vent 1 was switched on at time $t^* = 0$; medium gray shows that the lava flows issued after vent 2 was switched on at time $t^* = 2$; and light gray shows that lava plumes issued after vent 3 was switched on at $t^* = 12$. All three vents ceased their volumetric flow at $t^* = 20$.

4.3. Dimensional Analysis

Dimensional analysis is based on the principle that physical-model parameters follow physical laws that are independent of the units used to measure relevant physical variables. Scale-model theory requires geometric, dynamic, and kinematic similarities between a model and its prototype so that the model description of corresponding or identical physical systems can be justified. Rheological similarity is an additional criterion [*Weijermars and*

Table 1. Dimensionless Parameters of Chao Lava Field Model

Source No.	Position x^*, iy^*	Strength m^*	Far-Field Flow Rate U_∞	Switch-On Time t^*	Switch-Off Time t^*
1	-0.8, $+1.8i$	0.2	0.28	0	20
2	0, 0	0.6	0.28	2	20
3	$+1.1$, $-1.3i$	0.3	0.28	12	20

Schmeling, 1986; *Weijermars*, 1989; *Weijermars et al.*, 1993]. For any known physical system, relevant physical quantities can be expressed in terms of fundamental physical dimensions. In the case of the source flow system modeled in this study, critical parameters are relative locations and flux strengths of sources and duration of their flow. Source locations are specified by length dimensions $[L]$ in the complex potential space, z. Duration of the flow is given by the time dimension $[T]$. Flux strength of the sources is expressed in dimensions of the surface area $[L^2]$ that is injected (or erupted) over time $[T^{-1}]$ with a finite thickness $[L]$, as specified by equation (B8b). Superposed background flow has dimensions of particle displacement $[L]$ over time $[T^{-1}]$.

Model parameters of dimensional quantities can be translated as follows. Length dimensions used in our analytical models are normalized by a characteristic length or scaling unit. Allowing the source spacing to be a measure of characteristic length scale d_0 can translate nondimensional positions $(x, iy)^*$ of sources in the model to dimensional units as follows:

$$(x, iy)^* = (x/d_0, iy/d_0). \tag{1}$$

Model time t^* can be translated to real time scales using the characteristic time unit t_0:

$$t^* = t/t_0. \tag{2}$$

Nondimensional model source strength m_s^* and dimensional strength m_s in nature are connected by

$$m_s^* = m_s t_0/d_0^2. \tag{3}$$

Nondimensional background flow rate U_∞^* relates to dimensional rate U_∞ by

$$U_\infty^* = U_\infty t_0/d_0. \tag{4}$$

Table 1 summarizes dimensionless flow parameters used in our model for formation of Chao lava fields. Table 2 shows translation of the model parameters to nature using scaling factors t_0 and d_0 and equations (1) through (4). Total model time $t^* = 20$ translates to a dimensional emplacement time of 20 years. For Chao flow flux rate of the sources is $Q_s = 2\pi h\, m_s$ using equation B8b. Using a typical coulee flow thickness of $h = 100$ m yields flux rates of $Q_1 = 0.12$ km^3/yr, $Q_2 = 0.38$ km^3/yr, and $Q_3 = 0.19$ km^3/yr. Over the total runtime, this scaling yields a volumetric output of 2.4 km^3 for Chao I, 7.4 km^3 for Chao II, and 3.8 km^3 for Chao III. Field mapping of Chao I and II yields an estimated combined coulee volume of approximately 22 km^3 [*de Silva et al.*, 1994]. Compared with thickness $h = 100$ m and volumetric output for Chao I and II of 9.8 km^3 in our model run, we can upscale to 22 km^3 by assuming an average coulee thickness of these fields of 225 m, which is congruent with that of the relatively high (350–400 m) downslope termination of the flows. Field mapping of Chao III suggests a total eruption volume of approximately 3 km^3 [*Guest and Sanchez*, 1969; *de Silva et al.*, 1994], and the difference in our model volume of 3.8 km^3 can be (partly) attributed to erosion or a lesser flow thickness —80 m instead of 100 m.

5. Discussion

An analytical model of multiple sources with a superposed far-field flow (due to a shallow slope) has been applied to explain the lateral advance of a high-viscosity lava flow (section 4). In spite of our simplifying

Table 2. Dimensional Rates of Chao Lava Field Prototype[a]

Source No.	Position x (km), iy (km)	Strength m (km^2/yr)	Far-Field Flow Rate U_∞ (km/yr)	Switch-On Time t (year)	Switch-Off Time t (year)
1	-0.8, $+1.8i$	0.2	0.28	0	20
2	0, 0	0.6	0.28	2	20
3	$+1.1$, $-1.3i$	0.3	0.28	12	20

[a]Scaling unit for length: $d_0 = 1$ km. Scaling unit for time: $t_0 = 1$ year.

assumptions, such as the neglect of frictional resistance at the base of the layer, the model is capable of reproducing the essential features of the Chao coulee's 2-D geometry. Hot magma of the Chao complex erupted as a largely homogeneous body of dacitic lava [*de Silva et al.*, 1994]. Although the viscosity-dependent buildup of boundary layers will have affected the local flow dynamics near boundary layers, our model suggests that the overall flow of the sheet is determined by the faster flow zone that is sufficiently far away from the boundary layers. The upper surface of the lava is in contact with air and is a free surface until cooling creates a stiffer lid; hotter lava below the surface flows fastest in a Poiseuille-like flow zone between the top and the lower boundaries at the solid rock base [*Basu et al.*, 2012].

The 2-D geometry of the Chao coulee was modeled by choosing a uniform far-field flow rate and different source strengths for the three vents from which lava was issued. The viscosity for the bulk of the lava that controlled the advance the Chao coulee sheet was not required as an input in our model. However, we can use our model to estimate the effective viscosity of the lava by adopting a linear viscosity model for Poiseuille flow of a fluid with internal gravity on a slope between two rigid boundaries (simplifying *Spurk and Aksel* [2008] and assuming maximum velocity u_{XMAX} occurs half way up from the bottom):

$$u_{XMAX} = \frac{\rho g \sin \alpha}{8\eta} h^2 \qquad \left(\text{m s}^{-1} \right), \tag{5a}$$

with lava orthogonal thickness, h; basal slope angle, α; gravity acceleration, g; lava density, ρ; and lava viscosity, η. The viscosity is now explicitly given by

$$\eta = \frac{\rho g \sin \alpha}{8 u_{XMAX}} h^2 \qquad \left(\text{kg m}^{-1} \text{ s}^{-1} = \text{Pa s} \right). \tag{5b}$$

Using $\rho = 2600$ kg/m^3 (hot lava; [*Basu et al.*, 2012]) $g = 9.8$ m/s^2, $\alpha = 4°$ [*de Silva et al.*, 1994], $h = 100$ m, and $u_{XMAX} = 0.3$ km/Ma gives a viscosity estimate of 2.3×10^{11} Pa s for lava in Chao coulee when it was emplaced. Our estimated viscosity is within the range of 10^9 to 10^{12} Pa s assumed for the internal lava viscosity of the Chao dacite flow based on morphological analogies with other coulees [*de Silva et al.*, 1994].

6. Conclusions

This study provides a concise illustration of the type of geophysical flow visualizations possible with the complex potential description offered by applied mathematics. One suite of models involves Darcy flow in a homogeneous granular medium. Generic examples outlined in this study are time tracking of the migration of plumes from a series of pollution sources or the design of optimal well spacing and relative strength of multiple water injection pressures in field-development plans for hydrocarbon production. Further Darcy flow applications are modeling of fluid circulation in geothermal-energy projects.

Another suite of applications includes non-Darcy flow of high-viscosity fluids and crystalline creep, which occurs in lava streams advancing from a series of extrusion vents (as well as in salt-feeder stocks creeping up the stratigraphy into salt canopies; see below). Our present simulation of the Chao lava field formation shows three individual vents (along an interconnecting fracture) issuing lava streams that coalesce into one large composite lava field. Dimensional analysis has demonstrated that the composite lava flows may well have been emplaced within a couple of decades.

This study is intended as a practical starting point for further in-depth studies. For powerful flow visualizations, the basic equations of Appendices A and B need to be translated to a plotting code (Matlab in our case), which is essentially simple but involves tedium and in-depth understanding of fluid mechanics and which is required to ensure that computational processing errors are avoided. The tracking of specific particle paths mandates proper scaling so that meaningful time contours can be mapped. If properly applied, the conceptual description of flows using the analytical method of complex potentials does not introduce any computational inaccuracies. For each particular application, the technique of exact solutions can provide a sophisticated tool for tailor-made flow simulations.

Complex potentials can also be used as a complementary tool for checking flow solutions produced by nonlinear numerical methods. Unlike the differentiations in numerical approximations in which limitations of grid resolution and numerical iterations may perturb model outcomes, conformal mapping solutions are exact. Complex numerical schemes cannot always control the error propagation that leads to computational instabilities. This

realization has increased interest in development of a new generation of hybrid flow models, which seek to increase computational stability and accuracy by combining analytical and numerical-flow descriptions (e.g., for hybrid groundwater models, see *Haitjema et al.* [2010]; for hybrid reservoir models, see *Jha et al.* [2012]).

Further applications are the modeling of salt creeping from source feeder stocks into salt canopies. Coalesced salt sources in the canopy tend to cloud seismic images and create pressurized sutures [*Shumaker et al.*, 2007; *Hudec and Jackson*, 2009]. These sutures may jeopardize well safety and accuracy when presalt hydrocarbon targets are being drilled, which is why further modeling is merited.

Appendices A and B provide the fundamental equations for modeling any geometrical arrangement of multiple source flows (or a mixture of sources and sinks) and include solutions for multiple source flows with or without a superposed far-field flow.

Appendix A: Basic Flow Description by Potential Function, Stream Function, and Complex Potential

A1. Mass Conservation and Potential Function

The requirement of mass conservation of flow of an incompressible continuum is fulfilled by the continuity equation:

$$\nabla \cdot u = 0. \tag{A1a}$$

The dot product of velocity vector u is divergence, which is a scalar number that shows whether the velocity field generates or wastes any mass at a given point. The equivalent expression in terms of the harmonic potential function, ϕ, is

$$\nabla^2 \phi = 0. \tag{A1b}$$

This is equal to the Laplace equation, written in Cartesian coordinates (for a 2-D flow with $\partial/\partial z = 0$ and applying the second-order differential $\nabla \cdot \nabla$):

$$\nabla^2 \phi = \frac{\partial^2 \phi}{\partial x^2} + \frac{\partial^2 \phi}{\partial y^2} = 0. \tag{A1c}$$

The corresponding Laplacian equation in polar coordinates is given by

$$\nabla^2 \phi = \frac{\partial^2 \phi}{\partial r^2} + \frac{1}{r}\frac{\partial \phi}{\partial r} + \frac{1}{r^2}\frac{\partial^2 \phi}{\partial \theta^2} = 0. \tag{A1d}$$

The function ϕ is a scalar potential of the velocity, and the velocity can be recovered from the gradient of ϕ:

$$u = \nabla \phi. \tag{A1e}$$

The gradient operator on ϕ delivers Cartesian velocity components [*Weijermars*, 1998]:

$$u_x = \partial \phi / \partial x; \tag{A2a}$$

$$u_y = \partial \phi / \partial y. \tag{A2b}$$

The polar velocity components are

$$u_r = \partial \phi / \partial r; \tag{A2c}$$

$$u_\theta = (1/r)(\partial \phi / \partial \theta). \tag{A2d}$$

A2. Irrotational Flow and Stream Function

The requirement of irrotational flow is fulfilled when the velocity curl (vorticity) is zero:

$$\nabla \times u = 0. \tag{A3a}$$

The cross product of the velocity field is 0 because it may not generate spontaneous acceleration in a noninertial flow. The equivalent expression in terms of the stream function, ψ, is

$$\nabla^2 \psi = 0. \tag{A3b}$$

The stream function is a velocity vector potential, and the velocity can be recovered from the cross product of ψ:

$$u = \nabla \times \psi. \tag{A3c}$$

The velocity components in Cartesian (x, y) space are delivered by the curl operator on ψ (in 2-D flows $\partial/\partial z = 0$):

$$u_x = \partial\psi/\partial y; \tag{A4a}$$

$$u_y = -\partial\psi/\partial x. \tag{A4b}$$

The velocity components in polar (r, θ) space are

$$u_r = (1/r)(\partial\psi/\partial\theta); \tag{A4c}$$

$$u_\theta = -\partial\psi/\partial r. \tag{A4d}$$

A3. Complex Potential and Complex Function in Complex Analysis of 2-D Flows

The complex potential ϕ (or $\Omega(z)$) in complex analysis (i.e., the calculus of complex valued functions; cf. *Olver* [2012]) links the potential function ϕ and the stream function ψ:

$$\Omega(z) = \Phi = \phi + i\psi \tag{A5}$$

The related complex function $F(\bar{z})$ is the conjugate of the complex potential:

$$F(\bar{z}) = \overline{\Omega(z)} = \phi(x,y) - i\psi(x,y) \tag{A6}$$

Differentiating $\Omega(z)$ with respect to z and then conjugating the result yields the Pólya vector field $\overline{V(z)}$, for which solutions exist in Cartesian (x,y) coordinates and polar coordinates [*Pólya and Latta*, 1974]. Of course, it is also possible to first differentiate $F(\bar{z})$ with respect to $\bar{z}$. Using $v_x = \frac{\partial\phi}{\partial x} = \frac{\partial\psi}{\partial y}$ and $v_y = \frac{\partial\phi}{\partial y} = -\frac{\partial\psi}{\partial x}$ gives

$$\overline{V(z)} = \overline{\frac{d\Omega(z)}{dz}} = \frac{\partial\phi}{\partial x} - i\frac{\partial\psi}{\partial x} = v_x + iv_y. \tag{A7a}$$

Hence, the complex velocity field $V(z)$ is given by

$$V(z) = \frac{d\Omega(z)}{dz} = \frac{\partial\phi}{\partial x} + i\frac{\partial\psi}{\partial x} = v_x - iv_y. \tag{A7b}$$

The related complex function $F(z)$ in the complex plane can be written as

$$F(z) = \phi(x,y) + i\psi(x,y). \tag{A8}$$

The independent complex variable z is given by $z = x + iy$ with $i = \sqrt{-1}$. The potential function $\phi(x,y)$ and stream function $\psi(x,y)$ are the real part $\Re(z)$ of z and the imaginary part $\Im(z)$ of z (which can be obtained by multiplying the real number with i). The real and imaginary parts are valid solutions for ϕ and ψ, and for these harmonic functions the Cauchy-Riemann equations will be automatically satisfied:

$$\partial u_x/\partial x = \partial u_y/\partial y; \tag{A9a}$$

$$\partial u_x/\partial y = -\partial u_y/\partial x. \tag{A9b}$$

The derivative of $F(z)$ with respect to z gives the vector field, which in Cartesian (x, y) coordinates is given by

$$V(z) = dF/dz = \frac{\partial\phi}{\partial x} + i\frac{\partial\psi}{\partial x} = u_x - iu_y. \tag{A10}$$

The two Cartesian velocity components can be expressed in polar coordinates (r, θ):

$$u_x = u_r \cos\theta - u_\theta \sin\theta; \tag{A11a}$$

$$u_y = u_r \sin\theta + u_\theta \cos\theta. \tag{A11b}$$

Substituting these expressions in equation (A11) gives the complex vector field in polar (r, θ) space:

$$V(z) = dF/dz = (u_r - iu_\theta)\exp(-i\theta) = \left(\frac{\partial\phi}{\partial r} - i\frac{1}{r}\frac{\partial\phi}{\partial\theta}\right)e^{-i\theta}. \tag{A12}$$

The primitive complex function $F(z)$ can be written as

$$F(z) = \phi(r, \theta) + i\psi(r, \theta). \tag{A13}$$

The useful property of complex analysis is that complex functions can be mapped onto certain imaginary domains and retain the proper geometrical dimensions of streamlines and potential planes. This technique enjoys somewhat of a revival in applied mathematics (see Appendices A and C). Flow descriptions by analytical expressions are especially powerful because the composition of two complex functions is also a valid complex function that can be applied to describe the superposed flow fields.

A4. Complex Analysis of a Uniform 2-D Flow

For any specific case of a flow description by complex analysis, the complex potential $W(z)$ is connected to a complex function $F(z)$. For example, the complex potential for a general uniform flow with velocity U_∞ is

$$W(z) = U_\infty z. \tag{A14a}$$

The corresponding complex function $F(z)$ in Cartesian coordinates is

$$F(z) = U_\infty(x + iy) = U_\infty x + iU_\infty y. \tag{A14b}$$

For cases where U_∞ is aligned with the x direction, potential and stream functions simplify to

$$\phi(x, y) = U_\infty x. \tag{A15a}$$

$$\psi(x, y) = U_\infty y. \tag{A15b}$$

The vector field in Cartesian (x, y) coordinates is given by equation (A7b):

$$V(z) = dF/dz = \frac{\partial\phi}{\partial x} + i\frac{\partial\psi}{\partial x} = U_\infty - i0 \Leftrightarrow u_x - iu_y. \tag{A16}$$

The two velocity components are

$$u_x = U_\infty; \tag{A17a}$$

$$u_y = 0. \tag{A17b}$$

In polar coordinates the complex function for uniform flow can be obtained by substituting $z = |z|\,e^{i\theta}$ (with modulus $|z| = r$):

$$W(z) = U_\infty r e^{i\theta}. \tag{A18a}$$

The corresponding complex function $F(z)$ in polar coordinates is (using Euler's equation $e^{i\theta} = \cos\theta + i\sin\theta$)

$$F(z) = U_\infty r\cos\theta + iU_\infty r\sin\theta. \tag{A18b}$$

The potential function and stream function are

$$\phi(r, \theta) = U_\infty r \cos\theta;$$ (A19a)

$$\psi(r, \theta) = U_\infty r \sin\theta.$$ (A19b)

The complex vector field given in Cartesian (x, y) coordinates by equation (A7b) can now be expressed in polar (r, θ) space:

$$V(z) = \mathrm{d}F/\mathrm{d}z = \left(\frac{\partial\phi}{\partial r} - i\frac{1}{r}\frac{\partial\phi}{\partial\theta}\right)e^{-i\theta} = (U_\infty\cos\theta - iU_\infty\sin\theta)e^{-i\theta} = (u_r - iu_\theta)e^{-i\theta}.$$ (A20)

The two velocity components are

$$u_r = U_\infty\cos\theta;$$ (A21a)

$$u_\theta = U_\infty\sin\theta.$$ (A21b)

Appendix B: Examples of Complex Potentials for Multiple Source Flows

B1. Single 2-D Source at the Origin

Consider a 2-D source flow with areal flux $Q_A = Q/h$ due to volumetric flux Q over a characteristic finite height h of the 2-D source (Figure B1). The source can be assigned a strength parameter $m = Q_A/2\pi = Q/2\pi\,h$ (m^2 s^{-1}). The complex potential for a 2-D source flow located in the origin $(0, 0)$ is

$$W(z) = m\ln z.$$ (B1a)

Substitution of $z = |z|e^{i\theta}$ with modulus $|z| = r$ gives the complex potential in polar coordinates:

$$W(z) = m\ln(re^{i\theta}) = m\ln r + m\ln(e^{i\theta}).$$ (B1b)

$$W(z) \Leftrightarrow F(z) = \phi(r, \theta) + i\psi(r, \theta).$$ (B1c)

Potential and stream functions are

$$\phi(r, \theta) = m\ln r.$$ (B2a)

$$\psi(r, \theta) = m\theta.$$ (B2b)

The conditions of incompressible and irrotational flow are fulfilled because $\nabla^2\varphi = 0$ and $\nabla^2\psi = 0$.

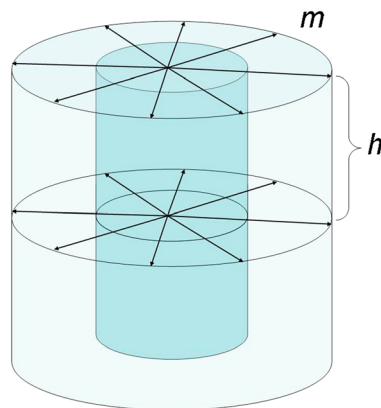The complex vector field for the 2-D source, in plane polar coordinates, is

$$V(z) = \mathrm{d}F/\mathrm{d}z = m/z = m/re^{i\theta} = (u_r - iu_\theta)e^{-i\theta}.$$ (B3)

The spatial velocity vectors (u_r, u_θ) in polar coordinates are

$$u_r = \frac{\partial\phi}{\partial r} = (m/r);$$ (B4a)

$$u_\theta = -\frac{1}{r}\frac{\partial\phi}{\partial\theta} = 0.$$ (B4b)

B2. Single 2-D Source and Doublet With Offset From Origin

The complex potential for a single 2-D source positioned at $(a, 0)$ is

$$W(z) = m\ln(z - a).$$ (B5a)

The vector field is

$$V(z) = m/(z - a).$$ (B5b)

Figure B1. Characteristic height h in 2-D source flow used to define flux strength m.

The above complex potential and complex vector fields are also valid for a 2-D source positioned at $a = (x_s, iy_s)$ and $z = (x, iy)$.

The complex potential for two 2-D sources (a doublet) positioned at $(0, a)$ and $(0, -a)$ is

$$W(z) = m \ln(z - a) + m \ln(z + a) = m \ln(z^2 - a^2).$$ (B6a)

Substitution of $z = |z|e^{i\theta}$ with modulus $|z| = r$ gives

$$W(z) = m \ln\left[(re^{i\theta})^2 - a^2 \right] = m \ln(x^2 - y^2 - 2ixy - a^2).$$ (B6b)

B3. Multiple 2-D Sources With Offset From Origin

For sources and sinks to be assigned to multiple locations in the (x, iy) domain, a concise formulation is merited and can be achieved by specification of the real and imaginary parts—x_s and y_s, respectively—of the source/sink. The complex potential of the 2-D vector field produced by n sources (positive m) or sinks (negative m) in the infinitely large complex plane is [*Potter*, 2008, p. 25]

$$W(z) = \sum_{s=1}^{n} m_s \log(z - z_s).$$ (B7a)

with spatial coordinates (x, y) in imaginary plane z and with strength $m = Q/2\pi$ with total fluid volume Q_{tot} generated at any radius equal to $Q_{tot} = m2\pi r$ (and with dimension $(m^3 s^{-1})$ due to unit length in the third dimension).

The complex vector field for a collection of point-source flows is given by a polynomial function of the form or complex series [*Brilleslyper et al.*, 2012, p. 206]:

$$V(z) = \sum_{s=1}^{n} m_s/(z - z_s).$$ (B7b)

The strength, m_s, of each source/sink has to be specified. The flux Q of a source is given by

$$Q = h \int_0^{2\pi} u_r r \, d\theta.$$ (B8a)

This equation assumes finite thickness of the flow so that h is a characteristic length. We now define strength m of the flow (positive for a source and negative for a sink) as

$$m_s = Q_s/2\pi h \qquad (m^2 \ s^{-1}).$$ (B8b)

The next step is to calculate all stream lines, but to do so we need to abstract the velocity vectors in x and y directions (u_x and u_y), which are given by $V(z) = u_x - iu_y$. For multiple sources we can obtain the velocity in x and y directions from the following derivation:

$$
\begin{aligned}
V(z) &= \sum_{s=1}^{n} \frac{m_s}{z - z_s} = \sum_{s=1}^{n} \frac{m_s}{(x + iy) - (x_s + iy_s)} \\
&= \sum_{s=1}^{n} \frac{m_s}{(x - x_s) + i(y - y_s)} \\
&= \sum_{s=1}^{n} \frac{m_s}{(x - x_s) + i(y - y_s)} \cdot \frac{(x - x_s) - i(y - y_s)}{(x - x_s) - i(y - y_s)} \\
&= \sum_{s=1}^{n} \frac{m_s((x - x_s) - i(y - y_s))}{(x - x_s)^2 + (y - y_s)^2} \\
&= \sum_{s=1}^{n} \frac{m_s(x - x_s)}{(x - x_s)^2 + (y - y_s)^2} - i \sum_{s=1}^{n} \frac{m_s(y - y_s)}{(x - x_s)^2 + (y - y_s)^2}.
\end{aligned}
$$ (B9)

From which it is immediately seen that

$$u_x = \sum_{s=1}^{n} \frac{m_s(x - x_s)}{(x - x_s)^2 + (y - y_s)^2}$$ (B10a)

$$u_y = \sum_{s=1}^{n} \frac{m_s(y - y_s)}{(x - x_s)^2 + (y - y_s)^2}.$$ (B10b)
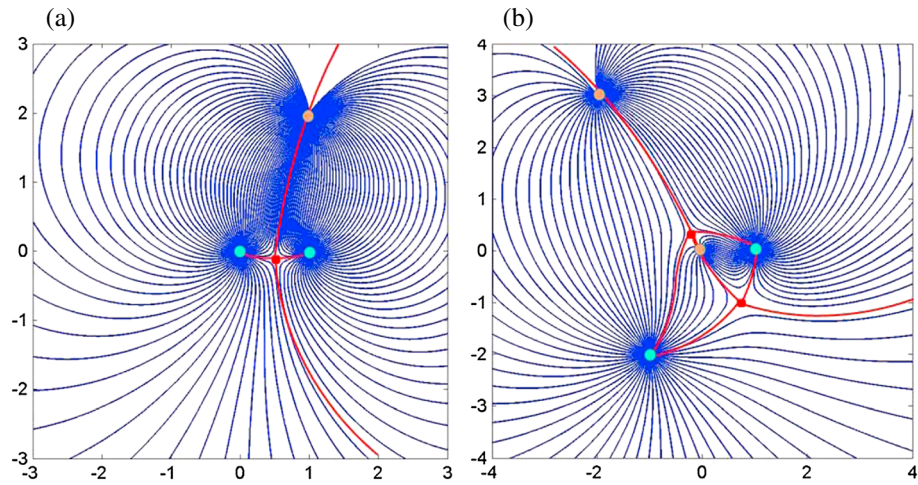
Figure B2. Integral curves corresponding to flow lines for vector fields around the multiple sources (blue dots) and sinks (orange dots) described by equations (B11) and (B12), respectively. Red curves are not crossed by any fluid. Red dots are stagnation points where fluid does not move at all. (a) Streamlines for flux strengths $m = 1, 1, -2$ at locations $z = 0, z = 1$, and $z = 1 + 2$. (b) Streamlines for flux strengths $m = 1, 2, -3/2$, and $-1/2$ located at $1, -1 - 2i, -2 + 3i$, and 0. (Based on examples given by *Brilleslyper et al.* [2012, p. 205] and *Potter* [2008, p. 26] and reproduced in our code).

These are the two velocity vectors (u_x and u_y) in x and y direction throughout the flow space, which thus describe the full vector field. These velocity components may be time dependent when any of the sources (m_s) is defined as a time-dependent variable, $m_{s(t)}$. The source flow field description can be superposed by a time-dependent $U_{\infty(t)}$ or constant U_∞ uniform flow. For example, assuming three-point sources (of relative strengths $m = 1, 1, -2$) at locations $z = 0, z = 1$, and $z = 1 + 2i$ (Figure B2a), the analytical function of equation (B7b) reduces to [*Brilleslyper et al.*, 2012, p. 204]

$$V(z) = (m_1/z) + [m_2/(z - 1)] + \{m_3/[(z - (1 + 2i)]\}. \tag{B11}$$

The complex potential of four-point sources (actually two source and two sinks of relative strengths $m = 1, 2, -3/2$, and $-1/2$) located at $1, -1 - 2i, -2 + 3i$, and 0 (Figure B2b) in complex plane z is [*Potter*, 2008]

$$W(z) = \ln(z - 1) + 2\ln(z - (-1 - 2i)) - \frac{3}{2}\ln(z - (-2 - 3i)) - \frac{1}{2}\ln(z). \tag{B12}$$

B4. Multiple 2-D Sources With Boundaries by Conformal Mapping

Complex analysis of physical flows in the z plane provides a description of flow lines in an unbounded domain, which can be denoted by the complex space C. Conformal mapping is a mathematical operation that can be utilized to create virtual boundaries (usually frictionless) in the flow domain. This mapping is achieved by a one-to-one complex-function mapping of some region in the z plane of complex space C to a connected domain in the w plane of complex half space H, making use of the Riemann Mapping Theorem. This theorem states that every simple, connected domain in the complex plane, with the exception of the entire plane, can be conformally mapped to the upper half plane $H = \{z|Im\ z > 0\}$ [*Brilleslyper et al.*, 2012]. The complex potentials for the H space remain similar (identity functions) to those of the C space, as long as the real axis (x axis) acts as the virtual boundary of the flow. Additional boundaries in the flow domain can be introduced, in which case a potential function in the C space is connected by a different complex potential function valid for a limited domain in the conformal mapping space (e.g., Disc Space D, Riemann Sphere S, and Joukowski Map J). The analytical functions are conformal at all points in their flow space, in which the derivative is larger than 0. The superposition of any complex analytical functions that are conformal mapping solutions is also analytic in the composite flow space. These complex functions must be harmonic functions to ensure valid solutions of the Laplace equation.

The principle of superposition and conformal mapping can now be applied to plot the streamlines for source flows with virtual boundaries (zero flow across). The complex potential for three-point sources, with relative

(a)   (b)
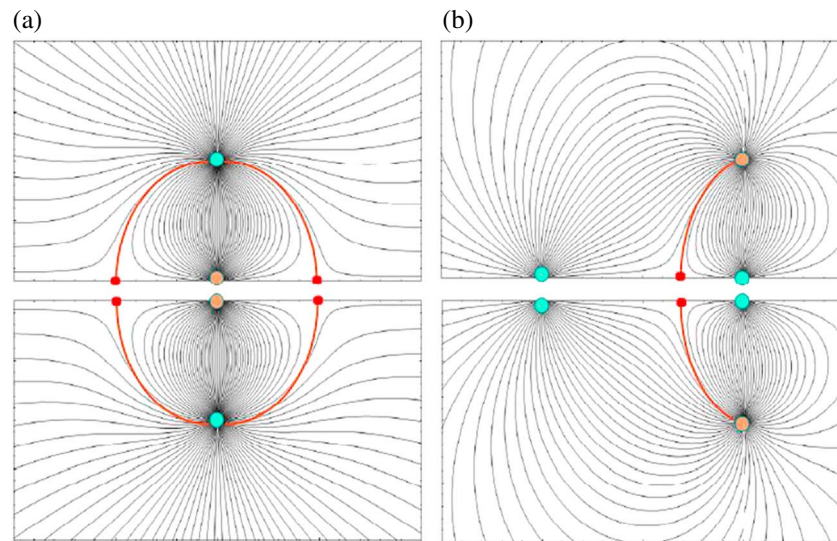
Figure B3. (a, b) Integral curves corresponding to flow lines for the vector fields around the multiple sources (blue dots) and sinks (orange dots) described by equations (B13) and (B14), respectively. Absence of fluid flow across the upper and lower halves of the flow space can be interpreted as solid boundaries [after *Potter*, 2008, pp. 29, 30]. Red curves are not crossed by any fluid either and confine fluid moving into the sink in Figure B2a. Red dots are stagnation points where fluid remains immobile. The unlimited complex space C can be conformally mapped in the upper flow space H confined to the z plane ($H = \{z | Im\ z\} > 0$).

strengths $m_1 = 1$ (source), $m_2 = 1$ (source), and $m_3 = -1$ (sink) located at $-i$, $+i$, and 0, respectively (Figure B3a) [after *Potter*, 2008, p. 28], is

$$W(z) = \ln(z^2 + 1) - \ln(z).$$ (B13)

The complex potential for four-point sources, with relative strengths $m_1 = 1$, $m_2 = 1$, $m_3 = -1$, and $m_4 = -1$ located at -1, $+1$, $1 + i$, and $1 - i$, respectively (Figure B3b) [after *Potter*, 2008, p. 28], is

$$W(z) = \ln(z + 1) + \ln(z - 1) - \ln(z^2 - 2z + 2).$$ (B14)

For each of the two cases considered, there is a central symmetry axis for the upper and lower half of the flow space. Because material flow cannot occur across the symmetry surface, it can be interpreted as a physical boundary. For translation to a real situation, the strength of the source placed in the mirror-image plane is twice the strength of a source injected at a natural boundary. In other words, the flux strength of a real injection at the boundary must be half the rate used in the mirror-image method outlined and illustrated here.

References

Anderson, J. D. (1995), *Computational Fluid Dynamics: The Basics with Applications*, McGraw-Hill, New York.

Barenblatt, G. I. (1996), *Scaling, Self-Similarity and Intermediate Asymptotics*, Cambridge Univ. Press, Cambridge, U. K.

Basu, D., K. Das, and S. Self (2012), Numerical simulation and analysis of lava flow cooling, Report Contract NRC–02–07–006 to U.S. Nuclear Regulatory Commission, Washington, D. C.

Batchelor, G. K. (1967), *An Introduction to Fluid Mechanics*, Cambridge Univ. Press, Cambridge, U. K.

Braden, B. (1987), Pólya's geometric picture of complex contour integrals, *Math. Mag.*, *60*, 321–327.

Brilleslyper, M. A., M. A. Dorff, J. M. McDougall, J. Rolf, L. E. Schaubroeck, R. L. Stankewitz, and K. Stephenson (2012), *Explorations in Complex Analysis*, Mathematical Association of America Inc. MAA Service Center, Washington, D. C.

Chin, W. C. (2002), *Quantitative Methods in Reservoir Engineering*, Elsevier, Woburn.

Churchill, R. V., and J. W. Brown (1984), *Complex Variables and Applications*, 4th ed., McGraw-Hill, New York.

de Silva, S. L., S. Self, P. W. Francis, R. E. Drake, and R. Carlos Ramirez (1994), Effusive silicic volcanism in the Central Andes: The Chao dacite and other young lavas of the Altiplano-Puna Volcanic Complex, *J. Geophys. Res.*, *99*, 17,805–17,825.

Drazin, P. G., and N. Riley (2006), *The Navier-Stokes Equations: A Classification of Flows and Exact Solutions*, p. 199, Cambridge Univ. Press, Cambridge, U. K.

Gluchoff, A. D. (1993), Complex power series—A vector field visualization, *Math. Mag.*, *66*, 189–191.

Guest, J. E., and J. Sanchez (1969), A large dacitic lava flow in Northern Chile, *Bull. Volcanol.*, *33*, 778–790.

Haitjema, H. M. (1995), *Analytic Element Modeling of Groundwater Flow*, Academic Press, San Diego, Calif.

Haitjema, H. M., D. T. Feinstein, R. J. Hunt, and M. A. Gusyev (2010), A hybrid finite-difference and analytic element groundwater model, *Ground Water*, *48*, 538–548.

Hudec, M. R., and M. P. A. Jackson (2009), Interaction between spreading salt canopies and their peripheral thrust systems, *J. Struct. Geol.*, *31*, 1114–1129.

Hurst, W. (1991), Infill drilling in the Rotherwood Field, Harris County, Texas, *SPE Res. Eng.*, *6*, 502–507.

Jha, A. K., G. Bansal, P. Deendaya, and G. P. Sangwai (2012), A strategic approach for the development of next generation reservoir simulators, in *SPE Oil and Gas India Conference and Exhibition*, 28–30 March, 9 pp., Society of Petroleum Engineers, Mumbai, India, SPE 152426.

Joseph, D. D. (2003), Viscous potential flow, *J. Fluid Mech.*, *479*, 191–197.

Joseph, D. D. (2006), Potential low of viscous fluids: Historical notes, *Int. J. Multiphase Flow*, *32*, 285–310.

Joseph, D. D., and T. Y. Liao (1994), Potential flows of viscous and viscoelastic fluids, *J. Fluid Mech.*, *256*, 1–23.

Joseph, D. D., T. Funada, and J. Wang (2007), *Potential Flows of Viscous and Visco-Elastic Liquids*, Cambridge Univ. Press, New York.

Kelly, P., R. L. Panton, and E. D. Martin (1990), Three-dimensional potential flows from functions of a 3D complex variable, *Fluid Mech. Res.*, *6*, 119–137.

Kundu, P. K., and I. M. Cohen (2002), *Fluid Mechanics*, 2nd ed., Academic Press, San Diego, Calif.

Needham, T. (1997), *Visual Complex Analysis*, Oxford Univ. Press, Oxford , U. K.

Olver, P. J. (2012), Introduction to partial differential equations (in prep.), chap. 7, *Complex Analysis and Conformal Mappings*. [Available at http://www.math.umn.edu/~olver/pd_/cm.pdf.]

Pólya, G., and G. Latta (1974), *Complex Variables*, John Wiley & Sons, New York.

Potter, H. D. P. (2008), On conformal mappings and vector fields, Senior thesis, Marietta College, Marietta, Ohio.

Shaw, W. T. (2010), Complex variable methods for 3D applied mathematics: 3D twistors and the biharmonic equation, Working Paper V1.2, May, Department of Mathematics, King's College. [Available at http://arxiv.org/pdf/1005.4184v1.pdf.]

Shumaker, N., R. Lindsay, and J. Ogilvie (2007), Depth-calibrating seismic data in the presence of allochthonous salt, *Leading Edge*, *26*, 1442–1453, doi:10.1190/1.2805761.

Spurk, J. H., and N. Aksel (2008), *Fluid Mechanics*, 2nd ed., Springer, New York.

Strack, O. D. L. (1989), *Groundwater Mechanics*, Prentice-Hall, Englewood Cliffs, N. J.

Strack, O. D. L. (2003), Theory and applications of the analytic element method, *Rev. Geophys.*, *41*(2), 1005, doi:10.1029/2002RG000111.

Wang, C. Y. (1991), Exact solutions of the steady-state Navier-Stokes equations, *Annu. Rev. Fluid Mech.*, *23*, 159–177.

Wegert, E., and G. Semmler (2011), Phase plots of complex functions: A journey in illustration, *Not. AMS*, *58*, 768–780.

Weijermars, R. (1989), Experimental pictures of deformation patterns in a possible model of the Earth's interior, *Earth Planet. Sci. Lett.*, *91*, 367–373.

Weijermars, R. (1998), *Principles of Rock Mechanics*, 2nd ed., Alboran Science Publishing, Amsterdam, Netherlands. [Available at http://ocw.tudelft.nl/courses/applied-earth-sciences/principles-of-rock-mechanics/course-home/.]

Weijermars, R., and A. Poliakov (1993), Stream functions and complex potentials: Implications for the development of rock fabric and the continuum assumption, *Tectonophysics*, *220*, 33–50.

Weijermars, R., and H. Schmeling (1986,) Scaling of Newtonian and non-Newtonian fluid dynamics without inertia for quantitative modelling of rock flow due to gravity (including the concept of rheological similarity), *Phys. Earth Planet. Int.*, *43*, 316–330.

Weijermars, R., M. P. A. Jackson, and B. Vendeville (1993), Rheological and tectonic modelling of salt provinces, *Tectonophysics*, *217*, 143–174.

White, F. M. (2011), *Fluid Mechanics*, McGraw Hill, New York.

Zill, D. G., and P. D. Shanahan (2009), *A First Course in Complex Analysis with Applications*, 2nd ed., Jones and Bartlett, Boston, Toronto, London, Singapore.